
Princeton Plasma Physics Laboratory

PPPL-

PPPL-



Prepared for the U.S. Department of Energy under Contract DE-AC02-09CH11466.

Princeton Plasma Physics Laboratory

Report Disclaimers

Full Legal Disclaimer

This report was prepared as an account of work sponsored by an agency of the United States Government. Neither the United States Government nor any agency thereof, nor any of their employees, nor any of their contractors, subcontractors or their employees, makes any warranty, express or implied, or assumes any legal liability or responsibility for the accuracy, completeness, or any third party's use or the results of such use of any information, apparatus, product, or process disclosed, or represents that its use would not infringe privately owned rights. Reference herein to any specific commercial product, process, or service by trade name, trademark, manufacturer, or otherwise, does not necessarily constitute or imply its endorsement, recommendation, or favoring by the United States Government or any agency thereof or its contractors or subcontractors. The views and opinions of authors expressed herein do not necessarily state or reflect those of the United States Government or any agency thereof.

Trademark Disclaimer

Reference herein to any specific commercial product, process, or service by trade name, trademark, manufacturer, or otherwise, does not necessarily constitute or imply its endorsement, recommendation, or favoring by the United States Government or any agency thereof or its contractors or subcontractors.

PPPL Report Availability

Princeton Plasma Physics Laboratory:

<http://www.pppl.gov/techreports.cfm>

Office of Scientific and Technical Information (OSTI):

<http://www.osti.gov/bridge>

Related Links:

[U.S. Department of Energy](#)

[Office of Scientific and Technical Information](#)

[Fusion Links](#)

Core Transport of Lithium and Carbon in ELM-free Discharges with Lithium Wall Conditioning in NSTX

F. Scotti¹, V.A. Soukhanovskii², R.E. Bell¹, S. Gerhardt¹, W. Guttenfelder¹, S. Kaye¹, R. Andre¹, A. Diallo¹, R. Kaita¹, B.P. LeBlanc¹, M. Podestá¹ and the NSTX Team

Princeton Plasma Physics Laboratory, Princeton, NJ, US

Lawrence Livermore National Laboratory, Livermore, CA, US

E-mail: fscotti@pppl.gov

Abstract. Core transport of intrinsic carbon and lithium impurities is analyzed in H-mode discharges in NSTX. The application of lithium coatings on graphite plasma facing components led to high performance H-mode discharges with edge localized mode (ELM) suppression and resulted in core carbon accumulation. Lithium ions did not accumulate and had densities less than 1% of carbon densities. Core transport codes NCLASS, NEO and MIST are used to assess the impact of lithium evaporative coatings on impurity transport. The disappearance of ELMs, due to changes in the electron pressure profiles, together with modifications in neoclassical transport, due to changes in main ion temperature and density profiles, explains the core carbon accumulation in discharges with lithium coatings. Residual anomalous transport in the pedestal region is needed to explain the experimental carbon density profile shape and evolution. The enhancement in neoclassical lithium particle diffusivities due to the high carbon concentration can be partially responsible for the low lithium core concentration.

1. Introduction

Impurity control is one of the major concerns for the applicability of high-performance ELM(edge localized mode)-free regimes in current and future magnetic confinement devices. Due to constraints on the lifetime of divertor materials in ITER, the number and the size of ELMs must be limited [1], potentially leading to impurity accumulation. The application of lithium evaporative coatings on graphite plasma facing components (PFCs) in the National Spherical Torus Experiment (NSTX) led to longer H-mode discharges with increased stored energy, suppression of ELMs and a concomitant core impurity accumulation (Z_{eff} increasing up to 4 and 50-60% of the total electron inventory due to carbon) [2, 3]. The achievement of ELM-free H-mode regimes in NSTX enabled the study of impurity sources, transport, and particle balances without the complications associated with ELMs.

Even if the PFCs are coated with lithium with typical thicknesses of tens of nanometers (corresponding to peak lithium areal densities of the order of 10^{21} atoms/m²), significant carbon sputtering is still observed as is evident from spectroscopic analysis of divertor carbon influxes. This appears to be due to the limited lifetime of lithium coatings due to erosion (under typical divertor ion fluxes of up to 10^{23} ions/m²/s), intercalation in graphite, toroidal asymmetries in lithium deposition, exposure of leading edges of the lower divertor graphite tiles, and incomplete poloidal coverage of lithium coatings. Carbon is the main core impurity of NSTX H-mode plasmas with its contribution to core Z_{eff} ($\Delta Z_{eff}^C = Z_C (Z_C - 1) n_C / n_e$, where $Z_{eff} = 1 + \sum_I \Delta Z_{eff}^I$) increasing up to 3 through typical discharges and its accumulation causing a lack of density control. This can be seen in Figure 1, where ΔZ_{eff} for different impurities and P_{rad} from over 100 high-triangularity ($\delta = 0.65 - 0.85$), high-elongation ($\kappa = 2.2 - 2.6$) ELM-free discharges are shown in a scatter plot at different times (right panels) together with the temporal evolution (left panels) from a typical discharge. The line-averaged density increases through the discharge and, while the deuterium inventory (not shown) is generally controlled, carbon density continues to ramp resulting in increasing Z_{eff} . Lithium concentration in the core is negligible, contributing less than 0.005 to Z_{eff} [5]. Metal impurity accumulation is also observed, which leads to a core radiated power up to 50% of the injected power while contributing less than 0.4 to Z_{eff} [6].

In this paper, neoclassical core impurity transport regimes and the agreement between neoclassical transport and the experimental transport levels for carbon and lithium are examined. The paper is organized as follows: in Section 2, experimental techniques and analysis codes are presented; in Section 3, neoclassical impurity transport regimes in NSTX H-mode discharges are examined; in Section 4, the difference in carbon transport in discharges with and without lithium conditioning is analyzed; and in Section 5, carbon and lithium transport levels are compared.

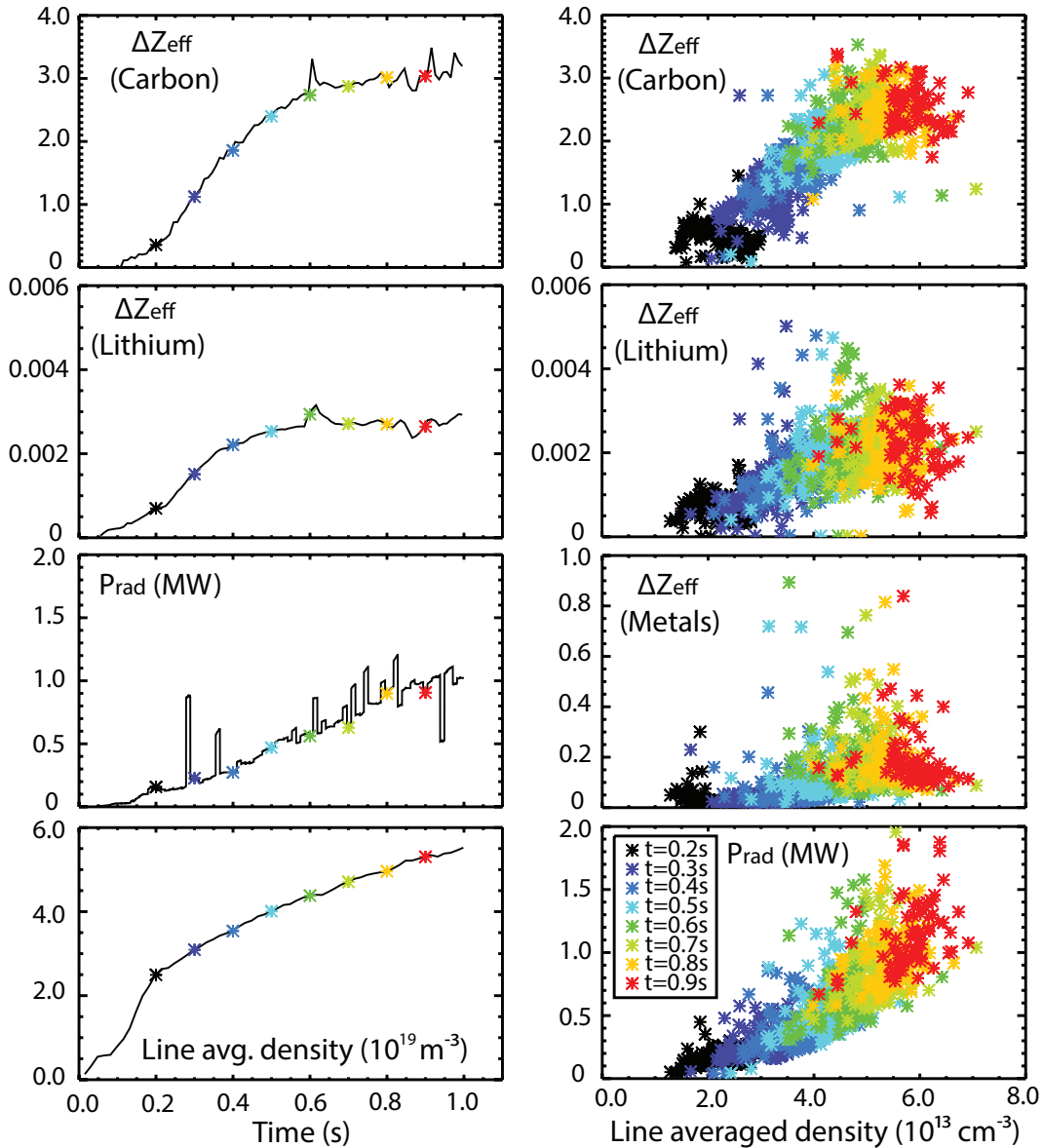


Figure 1. Contribution to Z_{eff} from main intrinsic impurities and core radiated power in NSTX H-mode NBI-heated ELM-free discharges shown in a scatter plot at different times (right) and in the time traces from a typical discharge (left).

2. Experimental techniques and analysis

NSTX is a large spherical tokamak with major radius $R = 0.85$ m and minor radius $a = 0.6$ m. Core impurity densities (carbon and lithium) are measured by charge exchange (CX) recombination spectroscopy (C-CHERS, Li-CHERS) [5, 7]. Carbon density profiles (n_C) are obtained from the C VI $n = 8-7$ transition at 529.1 nm while lithium density profiles (n_{Li}) are inferred from the Li III $n = 7-5$ transition at 516.7 nm. n_{Li} must be understood as an upper estimate of the core n_{Li} , typically within 50% [5], due to the contamination of the Li III CX line with a C VI line ($n = 14-10$). CHERS also provides ion temperature (T_i) and carbon toroidal rotation profiles (v_{tor}). Electron

temperature (T_e) and electron density (n_e) profiles are measured by the Multi Pulse Thomson Scattering (MPTS) system [8].

To explain core impurity behavior in tokamaks, both neoclassical (collisional) and anomalous transport typically need to be taken into account, with collisional transport providing the baseline level of particle transport [9, 10, 11, 12, 13, 14, 15, 16]. However, in spherical tori (ST), impurity transport proved to be close to the neoclassical levels both in CDX-U ohmic L-mode discharges (intrinsic impurities) [17] and in NSTX NBI-heated H-mode discharges (as shown by perturbative experiments with extrinsic impurities) [18, 19, 20]. In NSTX this is expected to be due to the suppression of ion scale microturbulence by the strong toroidal flow shear. Consistently, the ion thermal transport is also generally close to the neoclassical levels in H-mode discharges [21, 22], with deviations observed in discharges with lower collisionality [23]. This paper examines the behavior of intrinsic impurities (carbon and lithium) in NSTX NBI-heated discharges with and without lithium conditioning on graphite PFCs.

In this work, the predicted and experimental levels of impurity transport are evaluated using the transport codes NCLASS [24], NEO [25] and MIST [26]. NCLASS is a neoclassical code which uses the Hirshmann-Sigmar [27] formulation of neoclassical theory based on a fluid-moment approximation to calculate local neoclassical transport properties of a multi-species axisymmetric plasma of arbitrary aspect ratio, geometry and collisionality. NEO is a δf local neoclassical code which provides first principles numerical calculations of neoclassical transport. NEO is run using the full linearized Fokker-Plank collisional operator [28] and includes general geometry effects, finite orbit width effects and effects of toroidal rotation on equilibrium densities and radial fluxes [29]. Impurity toroidal velocities v_{tor} faster than thermal velocities v_{th} can cause poloidal redistribution of the impurity density and enhance neoclassical radial fluxes [30, 31, 32, 33], without, however, affecting the ratio of the diffusive and convective components. In order to determine the poloidal redistribution of ion densities, NEO solves the zeroth order non-linear Poisson equation for a multi-species rotating plasma, where the density for an ion species s on a given flux surface can be expressed as in [29]:

$$n_{0s}(\theta) = n_{0s}(\theta_0) \exp \left(-\frac{eZ_s}{T_{0s}} \Phi_*(\theta) + \frac{\omega_0^2 [R^2(\theta) - R^2(\theta_0)]}{2v_{th,s}^2} \right), \quad (1)$$

where $\Phi_*(\theta) = \Phi_0(\theta) - \Phi_0(\theta_0)$, Φ_0 is the electrostatic potential, $n_{0s}(\theta_0)$ is the density at the outer midplane (θ_0) taken as a input and ω_0 is the angular rotation frequency. MIST is an impurity transport code that solves the continuity equation in cylindrical geometry for every impurity charge state (here, the volumetric radius $r_{VOL} = \sqrt{\frac{V}{2\pi^2 R_0}}$ is used as radial coordinate in MIST calculations). MIST is run in semi-predictive and in fully-predictive modes. In semi-predictive simulations, MIST is run in time-dependent mode and the transport coefficients D (particle diffusivity) and v (convective velocity) are adjusted to match the time evolution of the impurity profiles. Once the best fit with the experimental data is obtained, this yields an estimate of the experimental transport coefficients. In fully-predictive simulations, the transport coefficients D and v are input

from neoclassical codes (NCLASS and NEO) and MIST is run in time-dependent mode to predict the evolution of the impurity profiles for the given neoclassical transport. In both cases, the impurity source is unknown and, while the time dependence of the source is assumed to be consistent with that of wall and divertor impurity influxes, the absolute values are scaled to match the total impurity inventories in the core.

As a consequence of centrifugal effects, the midplane impurity density (which is generally measured experimentally) can deviate from the flux surface averaged value, which is to be compared with predictions from theory (e.g. neoclassical, gyrokinetics). In NSTX H-mode plasmas, carbon v_{tor} often exceeds v_{th} in the core region [7] and asymmetries between the high field side (HFS) and low field side (LFS) n_e profiles are usually observed and have been associated with centrifugal effects [34, 35]. Consequently, the experimental impurity peaking factors (impurity density inverse gradient scale lengths) may differ whether they are evaluated on the LFS or on the flux-surface-averaged profiles. Here, the NEO code is used to estimate poloidal asymmetries of the impurity and main ion densities due to centrifugal effects. An example is shown in Figure 2 for a discharge analyzed later in this paper (129014, $t=0.58$ s with v_{tor} up to $\sim 1.75v_{th}$ for $r/a \leq 0.5$). In the left panel, the 2D poloidal asymmetry of impurity density is plotted as calculated by NEO; in the right panel experimental densities (black), experimental densities mirrored with respect to the magnetic axis (blue) and densities as calculated by NEO (red) are shown for electrons (top figure) and carbon (bottom figure). NEO was run using only LFS profiles ($r/a \geq 0$) as input. The HFS n_D and n_C were calculated using NEO and n_e was derived from quasi-neutrality. NEO predicts a significant n_C redistribution (up to 40-50%) in the core with a negligible effect on the n_D profile. The reconstructed HFS profiles are in good agreement in the core region with the experimental profiles both for n_C (available only until $r/a \sim 0.2$ on the HFS) and for n_e . Therefore, in the rest of the paper, in cases where the centrifugal effects can be important, the experimental impurity density gradient scale lengths will be evaluated on the flux-surface-averaged profiles (in green).

3. Transport regimes for main intrinsic impurities: carbon and lithium

In this section, the difference in neoclassical transport regimes for carbon and lithium is evaluated for an H-mode, ELM-free, NBI-heated (4-6 MW) discharge with lithium evaporative coatings (~ 200 mg). During ELM-free H-mode discharges, carbon density profiles have the typical behavior shown in Figure 3. A low concentration ($\sim 1\%$) peaked n_C profile in start-up typically evolves into a hollow n_C profile at the H-mode transition ($t \sim 0.1$ s). The steady slower core accumulation eventually leads to concentrations up to 10% and profiles peaked in the core and still evolving at the end of the discharge. A similar profile evolution is found for n_{Li} but with the extremely low values of $\sim 1\%$ of core n_C as upper limit, given the caveat of contamination in the lithium profiles.

In magnetically confined devices, neoclassical theory provides an enhancement of particle transport over the collisional level, due to the effects of trapped particles in

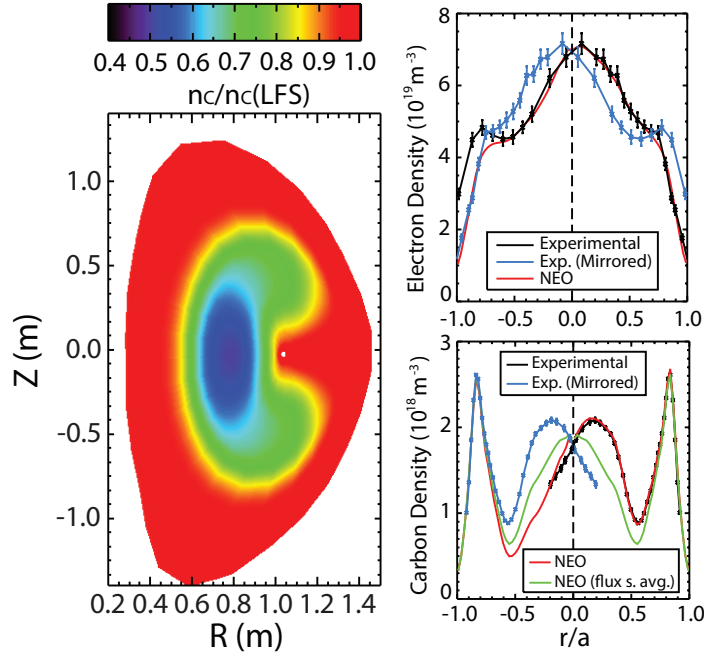


Figure 2. Left: estimated poloidal asymmetry of carbon density (129014, $t=0.580\text{s}$). Right-top: experimental n_e (black), experimental n_e mirrored with respect to the magnetic axis (blue) and midplane n_e as calculated by NEO (red). Right-bottom: experimental n_c (black), experimental n_c mirrored with respect to the magnetic axis (blue), midplane (red) and flux surface averaged (green) n_c as calculated by NEO.

a toroidal configuration. Collisionality regimes (in terms of $\nu^* \epsilon^{3/2}$, where $\epsilon = R/r$, $\nu^* = \frac{\nu R q}{v_{th} \epsilon^{3/2}}$, q is the safety factor and ν is the particle collision frequency), inter-species collision frequencies (where ν_{AB} is the test particle collision frequency of species A on species B) and impurity strength factors ($\alpha_Z = n_Z Z_Z^2 / n_D$) are important to understand neoclassical impurity radial transport. These are plotted in Figure 4 for an ELM-free H-mode discharge. Deuterium ions are in the banana-plateau (BP) regime while both carbon and lithium ions are in plateau regime in the core and in Pfirsch-Schlüter (PS) regime for r/a larger than respectively ~ 0.4 and ~ 0.6 . Lithium collision frequencies indicate the importance of including multi-ion effects [27, 37] for lithium transport. While carbon is a strong impurity (impurity strength $\alpha_C \geq 5$ at $r/a \sim 0.8$) mostly collisional on deuterium ions ($\nu_{CD} \sim 10^4 \text{ s}^{-1}$, $\nu_{CLi} \sim 5 \times 10^2 \text{ s}^{-1}$), lithium is a trace impurity ($\alpha_{Li} \leq 0.02$ at $r/a \sim 0.8$), mostly collisional on background carbon ions ($\nu_{LiD} \sim 5 \times 10^3 \text{ s}^{-1}$, $\nu_{LiC} \geq 10^4 \text{ s}^{-1}$). Thus, for carbon, ambipolarity in the neoclassical radial fluxes is satisfied to zeroth order in $\sqrt{m_e/m_D}$ with deuterium fluxes ($Z_C \cdot \Gamma_{r-C} = -\Gamma_{r-D}$).

Collisionality estimates and NCLASS analysis indicate that the inclusion of friction between multiple impurities due to the presence of lithium ions has a negligible effect

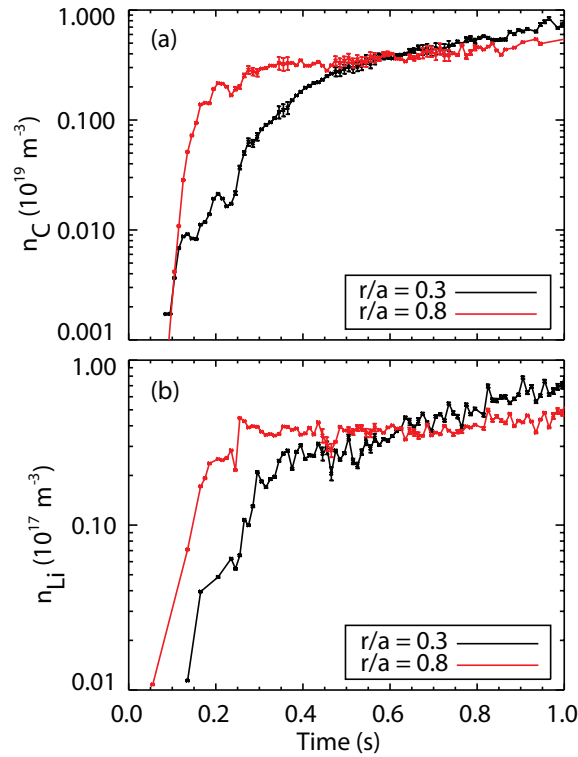


Figure 3. (a) Carbon and (b) lithium density evolution (discharges 130725, 130727). Note difference in scale between (a) and (b).

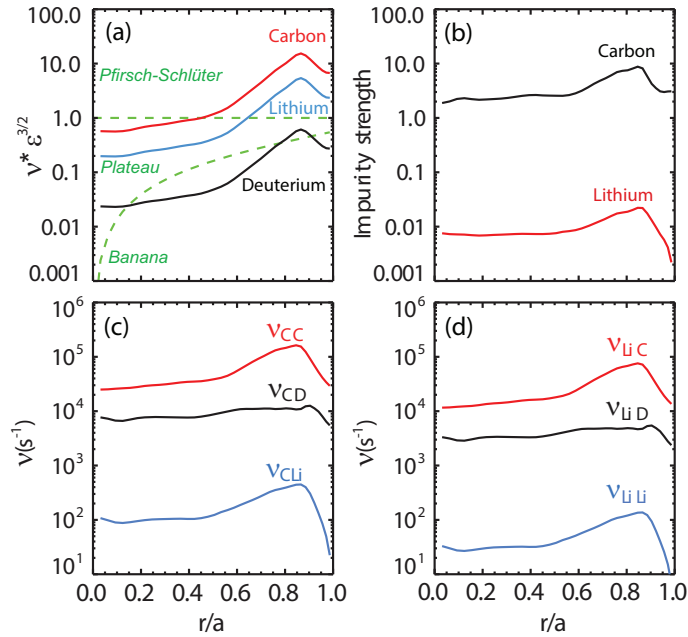


Figure 4. Carbon and lithium neoclassical collisionality regimes, collision frequencies and impurity strength factors (130725).

on carbon transport. The low lithium concentrations enabled a sensitivity study on n_{Li} (between $0.01\times$ and $100\times n_{Li-exp}$) using NCLASS, with minor perturbation to the

n_e profiles (adjusted for quasi-neutrality). The transport coefficients are calculated from the neoclassical impurity radial particle fluxes Γ_{r-Z} via a scan in the impurity density gradient. Diffusivity (D) and convective velocity (v) are obtained from the slope and the intercept of the linear fit of Γ_{r-Z}/n_Z versus $-\nabla n_Z/n_Z$ respectively and depend on the flux surface label choice (here $r/a = \frac{R_{mid-out} - R_{mid-in}}{R_{mid-out} + R_{mid-in}}$). In Figure 5, plasma parameters and transport coefficients are shown for the scan in n_{Li} . Here only the neoclassical components of the radial impurity fluxes (Pfirsch-Schlüter and Banana-Plateau) were included for the calculation of D and v . Effects on the neoclassical carbon transport can be seen only at $n_{Li} \sim 100 \times n_{Li-exp}$, at these lithium densities carbon would become predominantly collisional on lithium. Thus, the presence of lithium ions is not responsible for the increased carbon accumulation observed with lithium deposition.

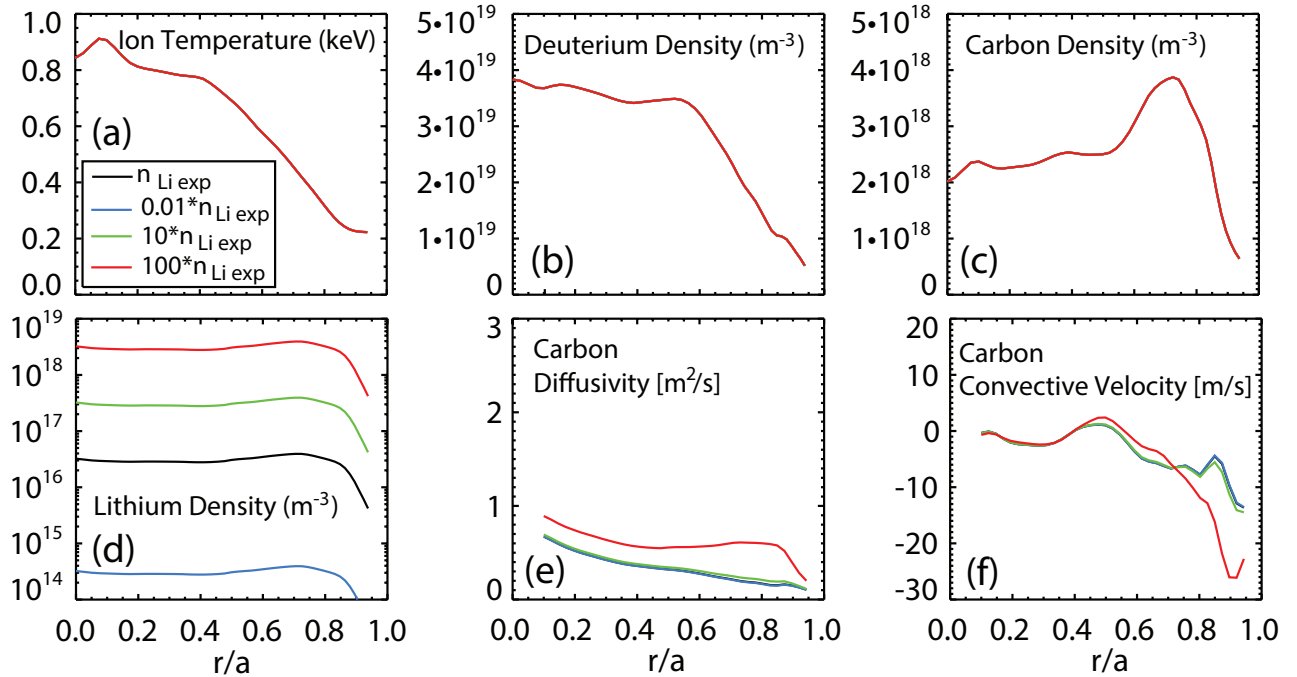


Figure 5. Modeling of the effect of varying n_{Li} (d) on neoclassical carbon transport coefficients (e,f) given main ion and impurity input profiles in (a,b,c).

Carbon neoclassical radial particle fluxes are mostly driven by friction on main ions. Due to the different neoclassical carbon collisionality regimes in the core and edge plasma (respectively Banana-Plateau and Pfirsch-Schlüter), all the components of the neoclassical fluxes need to be included. Considering only the contribution due to main ions, we can write approximate formulas for the classical (CL), banana-plateau (BP) and Pfirsch-Schlüter (PS) components of carbon radial particle fluxes and diffusivities as used in [12], following Hirshmann-Sigmar [27]:

$$\frac{\Gamma_{C-r}^{CL}}{n_C} = D_{C-r}^{CL} \frac{1}{a} \left[-\frac{a}{L_{nC}} + \frac{Z_C}{Z_D} \left(\frac{a}{L_{nD}} + H^{CL} \frac{a}{L_T} \right) \right], \quad (2)$$

$$\frac{\Gamma_{C-r}^{PS}}{n_C} = D_{C-r}^{PS} \frac{1}{a} \left[-\frac{a}{L_{nC}} + \frac{Z_C}{Z_D} \left(\frac{a}{L_{nD}} + \frac{H^{PS}}{K^{PS}} \frac{a}{L_T} \right) \right], \quad (3)$$

$$\frac{\Gamma_{C-r}^{BP}}{n_C} = D_{C-r}^{BP} \frac{1}{a} \left[-\frac{a}{L_{nC}} + \frac{Z_C}{Z_D} \left(\frac{a}{L_{nD}} + H^{BP} \frac{a}{L_T} \right) \right], \quad (4)$$

where the relevant diffusivities are:

$$D_{C-r}^{CL} = \frac{1}{(\partial\Psi/\partial r)^2} \left\langle \frac{R^2 B_p^2}{B^2} \right\rangle \frac{m_I k_B T \nu_{CD}}{e^2 Z^2}, \quad (5)$$

$$D_{C-r}^{PS} = \frac{\langle R B_T \rangle^2}{(\partial\Psi/\partial r)^2} \left(\langle B^{-2} \rangle - \langle B^2 \rangle^{-1} \right) K^{PS} \frac{m_I k_B T \nu_{CD}}{e^2 Z^2}, \quad (6)$$

$$D_{C-r}^{BP} = \frac{1}{(\partial\Psi/\partial r)^2} \frac{\langle R B_p \rangle^2}{\langle B^2 \rangle} \frac{m_I k_B T \mu_{CD}}{e^2 Z^2 n_C}, \quad (7)$$

where angle brackets indicate flux surface averaging, a is the minor radius, Ψ is the poloidal magnetic flux, L_{nD} , L_{nC} and L_T are respectively n_D , n_C and T_i gradient scale lengths ($a/L_x = a \frac{\partial \ln(x)}{\partial r}$) while ν_{CD} is the test particle collision frequency of carbon and deuterium, μ_{CD} is the weighted viscosity coefficient of impurity and main ion and the term H^{BP} is a function of the ratio of impurity and main ions viscosity coefficients as reported in [12]. For typical NSTX main ion collisionalities and impurity strengths, $K^{PS} \sim 1$ and $H^{PS} \sim -0.5$. The term H^{CL} in the classical fluxes is instead dependent on the impurity mass and charge and can be expressed as:

$$H^{CL} = - \left(\frac{3m_{CD}}{2m_D} - 1 - \frac{Z_D}{Z_C} \left(\frac{3m_{CD}}{2m_C} - 1 \right) \right) \quad (8)$$

where m_{CD} indicates the reduced mass of the carbon-deuterium ions system. For collisions between carbon and deuterium ions H^{CL} is then equal to -0.42. The ∇T_D term thus provides a screening term in both classical and PS fluxes, while a monotonically decreasing deuterium density profile would lead to an inward term in the impurity flux. It is clear from equations 2 and 3 that the CL and PS fluxes are characterized by approximately the same peaking (i.e., the ratio of convective to diffusive component of the radial fluxes), while the magnitude of the fluxes is proportional to the ratio of the classical and PS diffusion coefficient, which reduces to $D_{PS}/D_{CL} = \langle R B_T \rangle^2 \left(\langle B^{-2} \rangle - \langle B^2 \rangle^{-1} \right) / \left\langle \frac{R^2 B_p^2}{B^2} \right\rangle$. While this becomes $2q^2$ in the large aspect ratio circular plasma approximation, in a typical NSTX H-mode discharge this ratio reduces to the curve shown in Figure 6a as calculated from the geometrical factors (black curve) and by NCLASS (red curve). Therefore, in NSTX, due to the low

toroidal magnetic field, the classical and neoclassical processes can be of comparable importance. In Figure 6b and 6c, the relative contribution of CL, PS and BP fluxes to particle diffusivities and peaking factors is shown as a function of radius as calculated using NCLASS, confirming that carbon ions are in BP regime in the core and PS regime at the edge as determined before from collisionality estimates and indicating the importance of PS fluxes in providing an impurity screening component ($v/D \geq 0$).

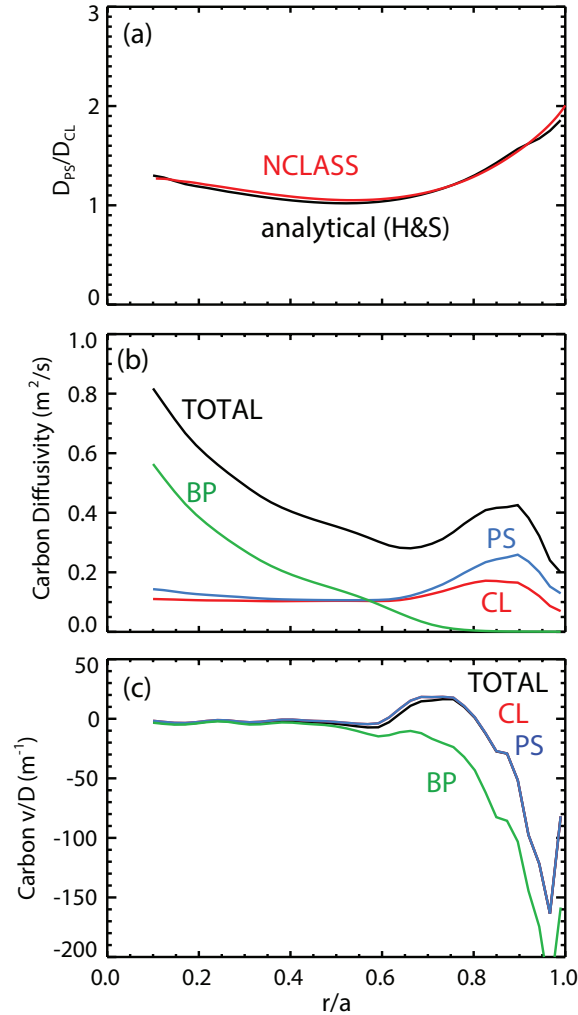


Figure 6. (a) Ratio of PS to CL carbon particle diffusivity; (b) and (c) contribution to impurity particle diffusivities and peaking factors due to CL, PS and BP components in a discharge with graphite PFCs (129014).

Lithium transport is, on the other hand, mostly driven by friction on carbon ions. While neoclassical codes are used in this paper to accurately derive the lithium transport coefficients, some insights on lithium transport characteristics can be derived from the simple equations for the neoclassical particle fluxes. First of all, for all the three neoclassical fluxes components (BP, PS and CL) the ratio of the convective component to the diffusive component scales with the charge of the impurity. This consequently leads to a reduced importance of the convective flux with respect to the diffusive flux for

the lithium-deuterium system if compared with the carbon-deuterium system. This is further reduced when collisions of lithium ions with carbon ions are important since the charge ratio between the two ion species is now 0.5. In the latter case (lithium transport dominated by collisions with carbon), we can also notice that the H^{CL} factor for lithium-carbon collisions changes sign so the typical *temperature screening* effect now turns into a weaker but inward pinch. Furthermore, the high background carbon density leads to the enhancement of lithium particle diffusivities, D_{Li} . From the Hirshmann-Sigmar formulation [27] for a trace impurity (lithium) in deep PS regime, we can compare the contributions to D_{Li} due to a background impurity (D_{Li-C}) and due to main ions (D_{Li-D}) from the evaluation of the two components of the diagonal matrix element L_{11}^{TT} from Equation 6.130d in [27]:

$$\frac{D_{Li-C}^{PS}}{D_{Li-D}^{PS}} = \frac{Y(m_{Li}/m_D)n_C Z_C^2 \sqrt{\frac{m_{Li}}{m_D}}}{n_D} \approx 1.04 \frac{n_C Z_C^2}{n_D}, \quad (9)$$

where $Y(m_{Li}/m_D)$ is a function of the impurity to fuel ion mass ratio. A carbon concentration of $\sim 3\%$ would cause a $\sim 100\%$ enhancement of D_{Li} . This is consistent with NCLASS results; the high edge carbon concentrations ($\sim 10\%$) in ELM-free discharges lead to enhanced D_{Li} and reduced peaking factors (v_{Li}/D_{Li}) as shown in Figure 7 where a sensitivity study in n_C is performed in several NCLASS runs. It is evident how decreasing n_c from the experimental levels leads to up to an order of magnitude reduction in lithium diffusivities.

In the next sections experimental and neoclassical transport levels are evaluated and compared for carbon (in discharges with and without lithium conditioning in Section 4) and for lithium (in lithiated discharges in Section 5).

4. Changes in core carbon transport with the application of lithium evaporative coatings

In this section, the changes in carbon transport between discharges with graphite PFCs and lithiated PFCs are studied, including the changes in neoclassical transport and the agreement between neoclassical predictions and experimental profiles as well as the role of ELMs in controlling impurity inventories. In Figure 8, waveforms from three discharges are shown, with the same shaping, NBI heating and plasma current (900kA): a discharge with graphite PFCs without any lithium applied beforehand (in black), a discharge run after 8 grams of lithium had been cumulatively evaporated in previous discharges but without any fresh lithium (in blue) and a discharge with 190 mg of fresh lithium deposited before the discharge (in red). Looking at the lower divertor D_α , the progressive reduction in recycling and disappearance of ELMs is evident. The latter was associated with changes in the pedestal electron pressure profile that were driven by changes in the electron density profiles [3, 4]. The beginning of the ELMing period is indicated in Figure 8 with a vertical dashed line. Medium size type-I ELMs in the discharge with graphite PFCs evolve into smaller amplitude, higher frequency ELMs

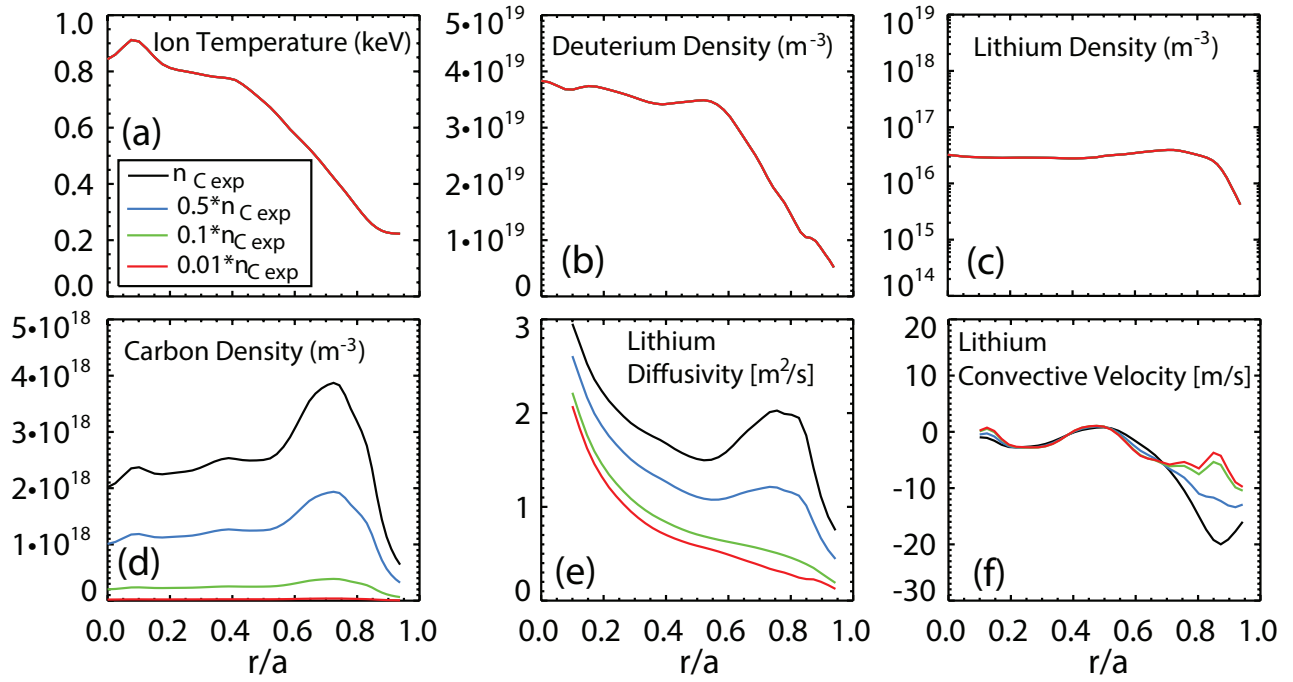


Figure 7. Modeling of the effect of varying n_C (d) on neoclassical lithium transport coefficients (e,f) given main ion and impurity input profiles in (a,b,c).

in the discharge without fresh lithium and are suppressed in the discharge with fresh lithium. Analysis of particle inventories (Figure 8-c, d, e) indicates how discharges with lithium application result in an increase in core carbon inventories by as much as a factor of 3-4. While the carbon inventory evolution in the discharge without fresh lithium is very similar to that in the ELM-free discharge, indicating a marginal impurity flushing effect associated with small ELMs, impurity inventories in the discharge without lithium start deviating from the ELM-free discharge at the beginning of the Type I ELM phase, possibly indicating significant impurity flushing due to ELMs. Spectroscopic analysis does not indicate an increase in divertor carbon influxes with the application of lithium coatings, suggesting an improvement in core impurity confinement (either due to change in ELM behavior or in baseline core/edge transport) and/or in edge impurity penetration (due to SOL parallel and perpendicular transport).

The changes in neoclassical core and edge carbon transport due to lithium conditioning will now be examined. As analyzed before, the contribution of lithium ions to carbon transport can be neglected, carbon is driven by friction with deuterium ions and changes in neoclassical carbon transport will be related to how lithium conditioning changes the deuterium temperature T_D and density n_D profiles, with the main drivers being the $\frac{\nabla T_D}{T_D}$ and $\frac{\nabla n_D}{n_D}$ components (Eq. 2, 3, 4).

Typical changes in ion profiles in discharges with lithium coatings with respect to discharges with graphite PFCs are an increase in n_C , an increase in the edge T_i , a reduction in n_D and its wider edge gradient. These changes can be seen in Figure 9, where the experimental profiles (T_e , n_e , T_C , n_c , n_D) for the discharge without

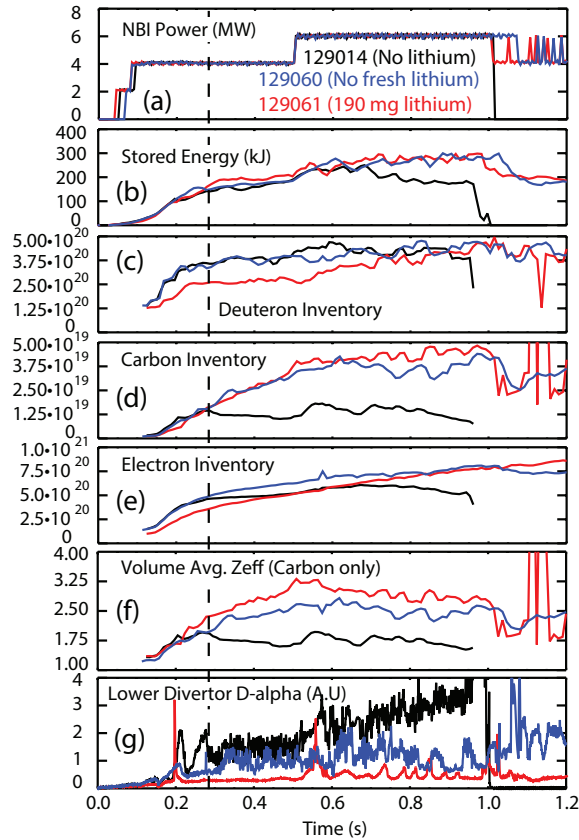


Figure 8. Waveforms of discharge parameters and particle inventories for a discharge with graphite PFCs (in black), a discharge run after 8 grams of lithium had been cumulatively evaporated in previous discharges but without any fresh lithium (in blue) and a discharge with 190 mg of fresh lithium deposited before the discharge (in red).

and with lithium are plotted together with the smoothed profiles used as input for the neoclassical analysis. The shadowed grey band ($0.85 \leq r/a \leq 1.0$) indicates the area with larger uncertainties in the main ion profiles and where extrapolation of the experimental profiles was done in the lithium-conditioned discharge. The reduction in the edge ∇T_D component (which provides impurity screening) and the wider ∇n_D component with lithium conditioning are clear in Figure 10 (top panels), where a/L_{nD} and a/L_T are plotted. This leads to a wider edge inward pinch that extends to r/a of 0.6 in discharges with lithium conditioning as evident from Figure 10 where the convective velocities (bottom-right panel) as well as particle diffusivities (bottom-left panel) are reported as calculated by NCLASS and NEO (including only PS and BP components). For comparison, in discharges without lithium the region with inward convective velocity extends as far as $r/a \sim 0.8$. An increase in inward convective velocity can also be observed in the core ($r/a \leq 0.2$) for discharges with applied lithium conditioning. Furthermore, the change in the edge T_D and n_D leads to a change in the carbon edge particle diffusivity which is reduced by a factor of 2 at $r/a \sim 0.8$. It must be noted also that NEO and NCLASS give consistent answers for both particle

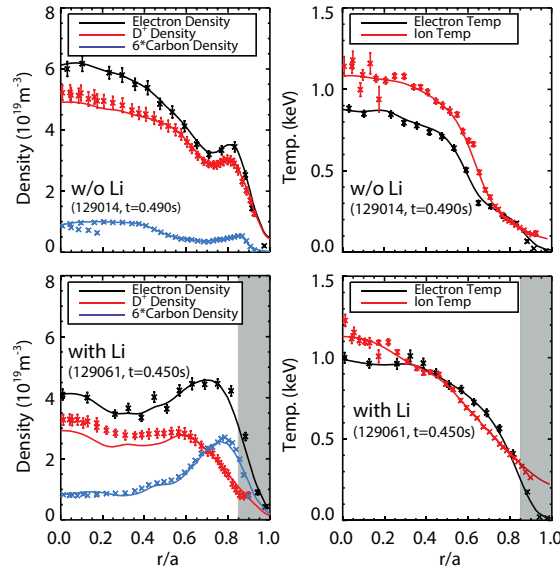


Figure 9. Profiles for discharges without (TOP) and with (BOTTOM) lithium conditioning.

diffusivities and convective velocities, with significant deviations appearing only in the core of the plasma where strong toroidal rotation causes enhancement of the transport coefficients.

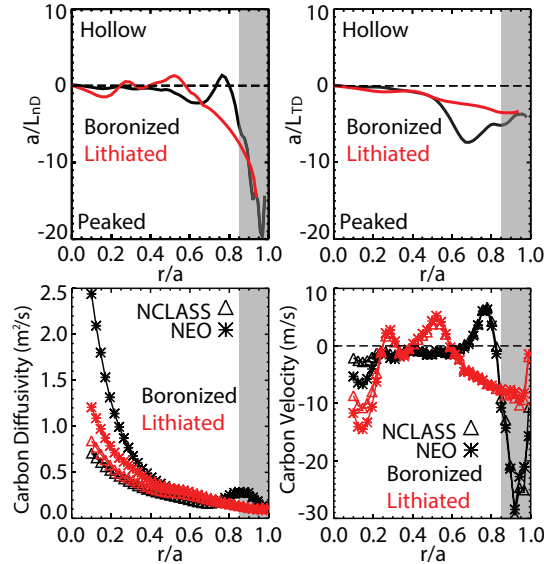


Figure 10. Gradient scale lengths and carbon neoclassical transport coefficients with and w/o lithium as calculated by NEO and NCLASS.

In order to verify the differences in impurity density profile shapes, evolution and accumulation due to changes in neoclassical transport as well as the agreement between neoclassical transport and the experimental profiles, the MIST code was run in fully predictive mode using as input particle diffusivities and convective velocities calculated

by NCLASS. The carbon edge source was assumed to be the same in the discharge with and without lithium coatings and was assumed to be a singly ionized carbon source at the separatrix adjusted so that the predicted MIST carbon inventory for the lithiated ELM-free discharge would match the experimental one. The results are shown in Figure 11 and 12 where the experimental n_C (a) and the n_C evolution as predicted by MIST (b), assuming neoclassical transport coefficients, are plotted versus radius and time for the discharge with graphite PFCs (Figure 11) and the discharge with evaporative lithium coatings (Figure 12). The neoclassical prediction for the discharge with graphite PFCs

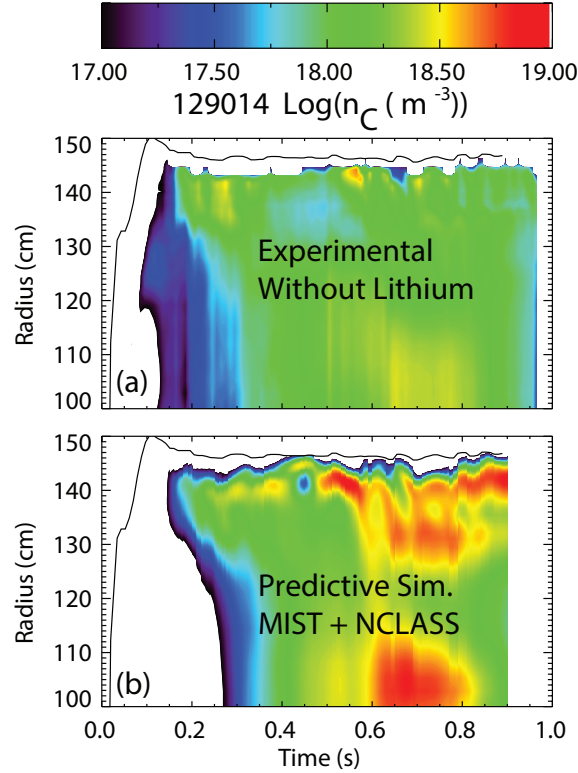


Figure 11. (a) Experimental carbon profiles and (b) simulated carbon profile for predictive NCLASS+MIST runs for a discharge without lithium conditioning.

is in reasonable agreement with the experimental profiles early in time and later develops edge peaking stronger than observed experimentally, with profile shapes consistent with experiment. The MIST neoclassically predicted carbon inventory keeps ramping during the discharge (due to accumulation for $r/a \geq 0.8$), with a density ramp rate similar to that in the lithiated discharge suggesting that, experimentally, the ELMs have an important role in keeping the edge carbon density and total carbon inventory flat over time (see Figure 8-d). The neoclassical prediction for the discharge with lithium coatings shows agreement in the early evolution of the discharge, predicting a highly hollow carbon profile as a result of a flat/slightly hollow n_D profile and a conventional T_i profile. For later times, neoclassical predictions indicate the location of the carbon edge density peak to be more inboard than observed experimentally and stronger core peaking than measured, with core accumulation.

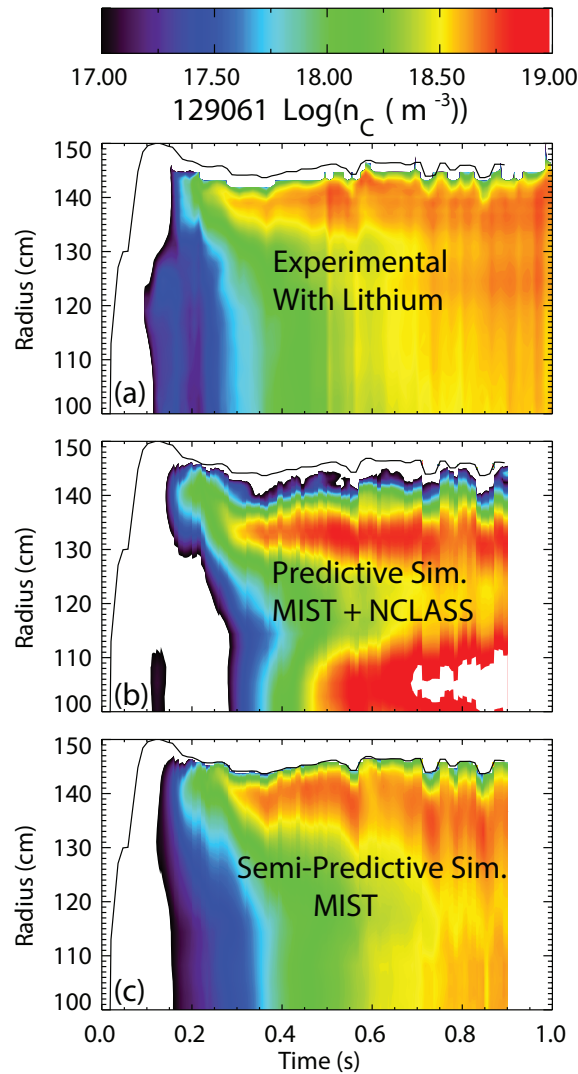


Figure 12. (a) Experimental carbon profiles, (b) simulated carbon profile for fully predictive NCLASS+MIST runs and (c) simulated carbon profile in semi predictive MIST simulation for a discharge with lithium conditioning.

While the profile evolution in discharges with lithium coatings is qualitatively consistent with neoclassical transport, some deviations with respect to experimental profiles are evident. This can be seen more clearly comparing the experimental peaking factors to the neoclassical predictions, as shown in Figure 13. In steady state in the source free region, the experimental peaking factors ($1/L_{nC}$) are equal to the ratio of the experimental convective velocity and diffusivity. A comparison of the experimental peaking factor with neoclassical predictions for the v/D ratio can give an estimate of the agreement of neoclassical transport with the experimental transport levels. It must be noted here that the total neoclassical and classical peaking factors are plotted in Figure 13. In particular, since classical fluxes are not calculated by NEO, the classical component is assumed to be the same as that calculated by NCLASS. The error bars for the neoclassical calculations were derived using a Monte Carlo method

to generate 50 different input profiles from the experimental profiles for T_i , n_e and n_C and running NEO on the randomly generated profiles. In the discharge with

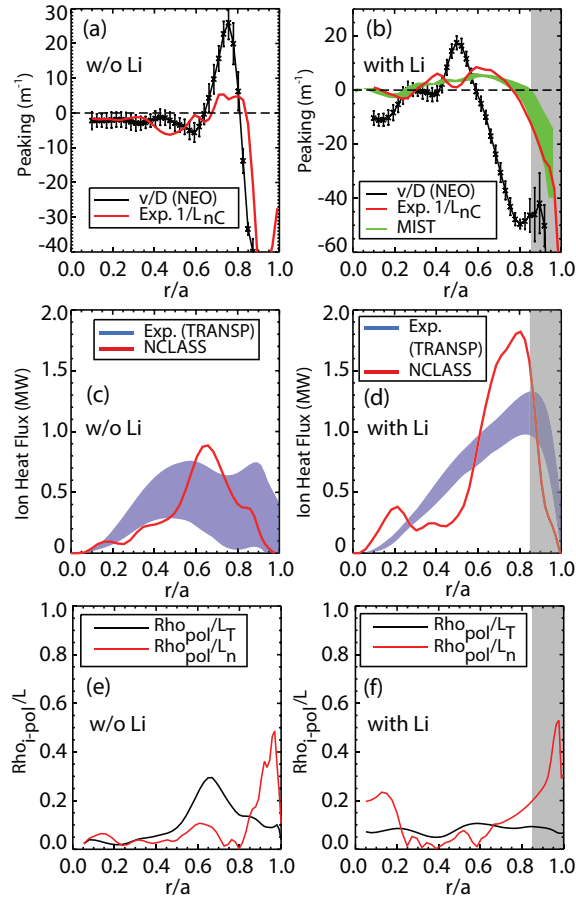


Figure 13. Comparison of discharges with graphite plasma facing components (a, c, e) and a discharge with lithium conditioning (b, d, f). Experimental and neoclassical carbon peaking factors (a, b), experimental and neoclassical ion heat fluxes (c, d) and neoclassical ordering of ρ_{i-pol} over gradient scale length (e, f).

graphite PFCs (Figure 13-a), the experimental peaking factors in red (evaluated on the flux surface averaged profiles calculated by NEO) are in very good agreement with the neoclassical predictions in black (by NEO) both in the core and edge with very good agreement in both regions of peaked and hollow profiles. Experimental profiles show, however, weaker edge peaking than expected from neoclassical estimates and this can be associated with the flattening/flushing role of ELMs, in agreement with previous conclusions from the predictive analysis. In the lithium conditioned discharge (Figure 13-b), qualitative agreement is found between the neoclassical predictions and the experimental peaking factors: an outward convection region ($0.2 \leq r/a \leq 0.6$) and a strong edge pinch. Deviations are observed at the pedestal top and in the core region. The different sign of the peaking factors at the pedestal top ($r/a \sim 0.7 - 0.8$) suggests either an anomalous convective contribution or a deficiency in the neoclassical model. This is further confirmed by semi predictive MIST simulations. The simulated

carbon density profiles are shown in the contour plot in Figure 12 (c) while the semi-predictive v_{MIST}/D_{MIST} is shown in Figure 13 in green. The semi-predictive simulation was carried out for the lithiated ELM-free discharge using neoclassical level diffusivity and adjusting the convective velocity in order to match the carbon density profiles. The good agreement obtained with the experimental profiles indicates the need for an anomalous convective contribution with respect to NCLASS calculations.

More insight on the possible reasons for this discrepancy can be obtained looking at ion thermal transport levels as well as the applicability of neoclassical theory. Ion scale microturbulence that could account for this anomalous convective flux is usually expected to be suppressed in NSTX due to the strong flow shear. Consistent with this, ion heat fluxes are usually well described by neoclassical theory [21]. Figure 13-c,d shows the integrated experimental ion energy fluxes (as calculated by TRANSP, including the conductive and convective component) and neoclassical ion energy fluxes (as calculated by NCLASS). While reasonable agreement is found in the magnitude of the heat fluxes, NCLASS fails to predict the heat flux profile shape both in the discharge with and without lithium conditioning (Figure 13-c,d). In the latter, in particular, the overestimation of the heat flux (at $r/a \sim 0.7-0.8$) is due to a large convective component predicted by NCLASS. These results are consistent with the deviations from the neoclassical levels in the ion thermal transport which were observed in lower collisionality H-mode discharges with lithium conditioning. In these cases ballooning type ion scale instabilities were predicted to occur which could possibly contribute to both thermal and particle transport [23]. It must also be noted that the deviation from the neoclassical level of transport are observed in regions where the neoclassical orderings (ρ_{pol}/L_x) are only marginally applicable as it can be seen in Figure 13-d,e where the ratio of poloidal gyroradius to gradient scale lengths are plotted. However, while this is expected to possibly alter transport in the banana-plateau regime, in this region neoclassical impurity transport is dominated by CL and PS contributions. Furthermore, uncertainties in the n_D profiles in discharges with lithium conditioning can lead to uncertainties in the derived neoclassical impurity transport coefficients. n_D profiles are not directly measured but are inferred from n_e and n_C assuming C^{6+} as the only significant impurity. Since at the pedestal top in an ELM-free discharge n_D can be less than 50% of n_e , the n_D profiles can be very sensitive to uncertainties in the impurity density.

MIST simulations can also give information on whether the change in the edge and core transport coefficients due to the application of lithium conditioning can be partially responsible for the increased core carbon inventories. Fully predictive MIST simulations, shown in Figure 12-b and 11-b, using neoclassical transport coefficients, the same edge source, the same effective SOL parallel transport and assuming SOL perpendicular transport coefficients equal to those at the separatrix, indicate that the change in the baseline neoclassical transport with lithium conditioning does not consistently lead to an increase in the core carbon inventory. Conclusions are further limited by the uncertainties in the assumptions for the SOL transport and in the n_D

profiles for r/a larger than 0.85 in discharges with lithium conditioning. However, the change in the neoclassical transport coefficients would lead to a deeper penetration of the impurities in the core where they are less sensitive to the flushing effect of ELMs. This is qualitatively consistent with the observation that ELMs triggered with 3D fields in discharges with lithium coatings were able to affect only the carbon density in the outer most volume of the plasma $r/a \geq 0.7$ [38]. This was effective in reducing the total carbon inventories but left the central accumulation unaffected. To first order then, ELMs in discharges without lithium conditioning appear to be responsible for keeping the total impurity inventory flat in time. Modeling of the effect of ELMs, both natural and triggered by 3D fields, on the impurity density evolution will be reported elsewhere.

5. Comparison of carbon and lithium experimental transport levels in discharges with lithium conditioning

In this section carbon and lithium neoclassical and experimental transport levels are compared in discharges with lithium conditioning. The main objectives are to understand whether lithium shows the same deviation from neoclassical behavior observed for carbon in discharges with lithium conditioning and if the differences with respect to carbon transport can help understand the very low core n_{Li} . A comparison of neoclassical transport coefficients for carbon and lithium is shown in Figure 14, including only the BP and PS contribution. The difference in transport coefficients for carbon and lithium ions is clear, with lithium showing an order of magnitude higher edge D (Figure 14-a) with comparable or higher inward edge v (Figure 14-b). This results in a weaker neoclassical impurity peaking for lithium than for carbon. NEO and NCLASS are in good agreement showing differences only inside of $r/a=0.6$ due to the effects of toroidal rotation that are neglected in NCLASS.

The agreement between neoclassical transport and the experimental transport levels is again investigated looking at the impurity peaking factors. Neoclassical predictions for the steady state peaking factors (v_{neo}/D_{neo}) are compared to the experimental peaking factor for both carbon and lithium in the source free region in Figure 15. Since the measured n_{Li} is as an upper estimate of the real n_{Li} , the profile shape and the gradient scale lengths might be only partially representative of the real n_{Li} profile. Furthermore, the shaded region in grey indicates the region with higher uncertainties in the ion profiles where extrapolation of the experimental profiles was done. It must be noted that due to their dependence on the profile gradients, the convective components are more sensitive to the uncertainties in the profiles. As shown in Figure 15 (left panels), for both lithium and carbon in the early stages of the discharge the experimental v/D are in good agreement with the neoclassical estimates. Both NEO and NCLASS predict a large region ($r/a \leq 0.8$) of outward convection which agrees with the experimentally observed early hollow impurity profiles. Later in the discharge (Figure 15, right panels), the neoclassical carbon peaking factor deviates from the experimental one as observed in the previous section (in a different discharge). Lithium behavior seems to be closer

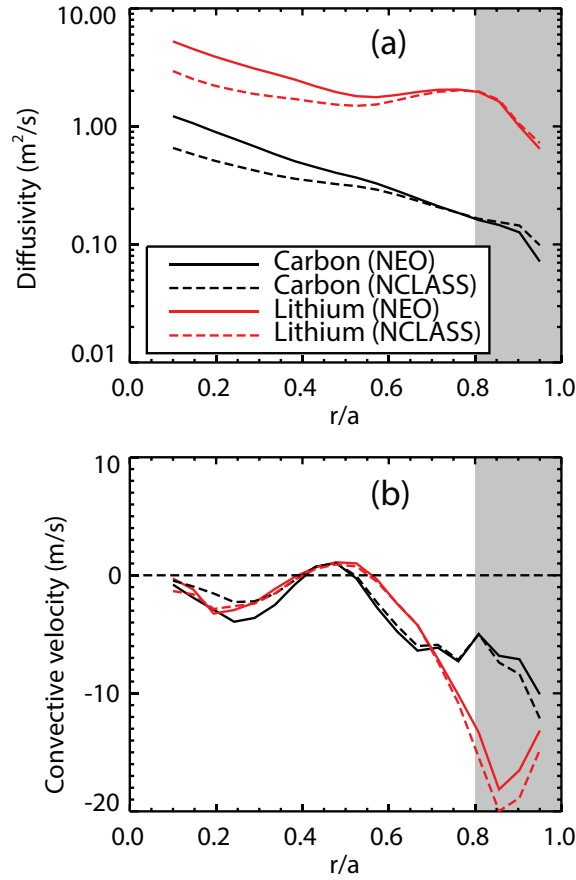


Figure 14. NEO and NCLASS calculation of radial transport coefficients for carbon and lithium.

to neoclassical predictions, possibly due to the higher neoclassical particle diffusivities. A comparable contribution to carbon and lithium transport due to turbulent transport would then have a weaker impact on lithium fluxes. In Figure 15, the red vertical bars are representative of the error bars for the neoclassical calculations in the non-shaded regions.

Let's now try to determine whether the differences in the core transport between carbon and lithium can explain the difference in the core inventories ($N_{\text{Li}}/N_{\text{C}} \leq 0.01$). In Figure 16, carbon and lithium experimental density profiles are plotted for $0.8 \leq r/a \leq 1.0$ normalized to their value at $r/a = 0.8$ at several times during a discharge. It must be noted that here a zeroth order correction was applied to the lithium profiles in order to correct for the carbon contamination. The brightness of the C VI $n = 14 - 10$ transition was derived from the brightness of the $n = 8 - 7$ transition as described in [5] and then subtracted from the contaminated Li III brightness to obtain a more accurate lithium density profile. Applying this correction further reduces the core lithium densities, with a difference in the density normalization factors between carbon and lithium at $r/a = 0.8$ of a factor between 100 and 300. Carbon density profiles show a decrease of a factor of ~ 100 from $r/a = 0.8$ to $r/a = 1.0$ while lithium density profiles have a weaker decay

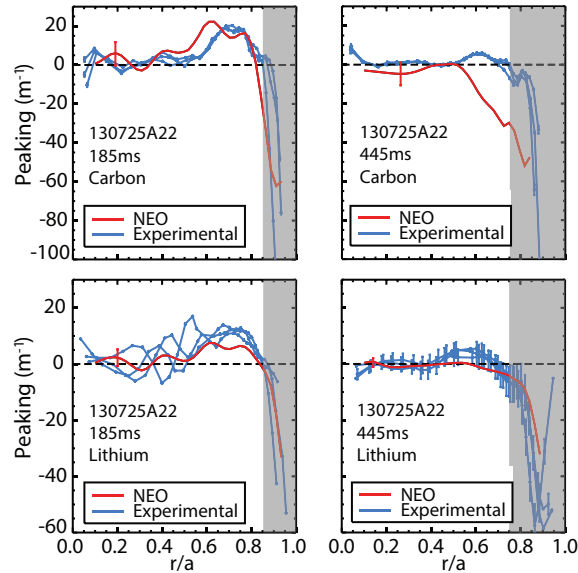


Figure 15. Peaking factors for carbon (top) and lithium (bottom) for 130725 at $t=200$ ms (left) and $t=445$ ms (right). Experimental peaking factors for three different time points around the time of interest are plotted in blue and neoclassical peaking factors as calculated by NEO are plotted in red.

with $n_{Li}(r/a = 1.0)/n_{Li}(r/a = 0.8) \sim 0.1$. The difference in the carbon and lithium experimental profiles suggests that edge radial transport is partially responsible for the low core lithium density. However, the fact that edge radial transport can account only for a factor of about 10 in the n_{Li}/n_C ratio indicates that differences between lithium and carbon sources and parallel SOL transport must also be playing a role. In order to determine how much of the difference between the two impurities edge radial profiles can be due to neoclassical transport, we can calculate $\int_{r/a=1.0}^{r/a=0.8} (v/D)_{neo} dr$ which gives the density at $r/a = 0.8$ normalized by the density at the separatrix for both carbon and lithium as a result of the neoclassical v/D . Carbon densities at $r/a = 0.8$ predicted in this way are up to ~ 1000 times higher than the lithium densities, with uncertainties due to the uncertainties in the neoclassical transport coefficients in the plasma edge. This indicates that neoclassical transport could potentially be enough to explain the core differences observed between carbon and lithium but this effect is effectively reduced as a result of the apparent non-neoclassical behavior of carbon in the plasma edge.

Work on the differences between carbon and lithium sources and SOL transport is ongoing and will be reported elsewhere. The reduction in lithium sources needed to account for the further reduction in core concentrations can be the result of the large fraction of redeposited lithium ions due to the very short ionization mean free path (smaller than the ion gyroradius), the better entrainment in the divertor of the sputtered lithium due to the differences in the SOL parallel force balance (in particular in the ion temperature gradient force) and in the source profile (from UEDGE 2D multi-fluid simulations) and to the different poloidal distribution of impurity sources (lithium mostly concentrated in the lower divertor due to the LITER evaporation pattern; carbon

main chamber wall sources likely to still play an important role).

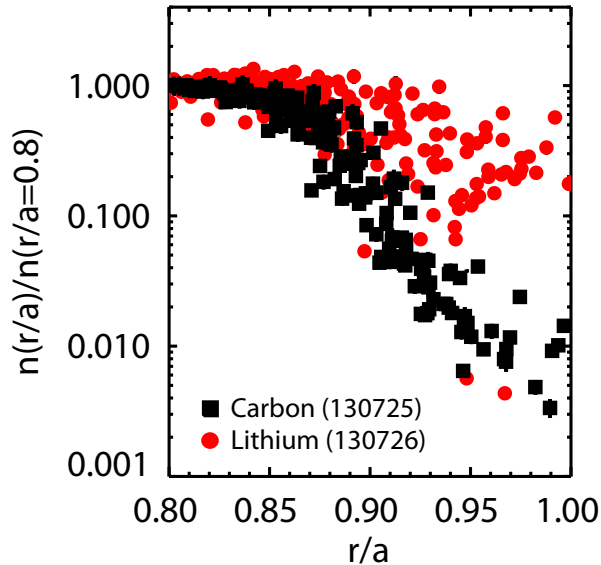


Figure 16. Carbon (black) and lithium (red) edge density profiles normalized by their values at $r/a = 0.8$. Profiles from a single discharge at several time slices between 0.35 s and 0.65 s during a discharge. The ratio of the normalization factors for carbon and lithium ranges between 100 and 300 at $r/a = 0.8$.

6. Summary

Neoclassical transport of intrinsic impurity (carbon and lithium) is analyzed for H-mode discharges in NSTX. ELM-free H-mode discharges are generally characterized by carbon accumulation. Lithium ions do not accumulate and have densities (n_{Li}) only up to 1% of carbon densities (n_C). Core transport codes NCLASS, NEO and MIST were used to assess the impact of lithium conditioning on impurity transport. The disappearance of ELMs together with changes in neoclassical transport due to modifications in main ion temperature (T_D) and density (n_D) profiles can explain the core carbon accumulation. However, residual anomalous transport is needed in order to reproduce the evolution of the n_C profiles. Possible unsuppressed turbulence, inaccuracy of neoclassical theory and uncertainties in main ion profiles could be at the origin of the observed discrepancies in carbon transport in lithium conditioned discharges and are now subject of more investigation. The enhancement in lithium particle diffusivities due to the presence of carbon can partially account for the low lithium core contamination. A reduction of the edge source of an order of magnitude if compared to the carbon edge source would still be needed in order to reproduce the extremely low n_{Li} observed in experiments. Work is ongoing for a better characterization of the difference between carbon and lithium impurity sources in NSTX discharges.

7. Acknowledgements

Work supported by U.S. DOE Contract DE-AC02-09CH11466 and DE-AC52-07NA27344. The authors would like to acknowledge Dr. Steve Sabbagh for EFIT calculations, Dr. Rajesh Maingi, Dr. Eric Meier and Dr. Alessandro Bortolon for useful discussions, Dr. Emily Belli and Dr. Jeff Candy for the availability of NEO code and useful discussions.

References

- [1] ITER Physics Expert Group on divertor, ITER Physics Expert Group on Divertor Modelling and Database, ITER Physics Basis Editors: Chapter 4: Power and particle control 1999 Nucl. Fusion **39** 2391.
- [2] M.G. Bell et al., Plasma Phys. Control. Fusion **51**(12), 2009.
- [3] R. Maingi, et al., Phys. Rev. Lett. **103** (7), 075001, 2009.
- [4] R. Maingi, et al., Nucl. Fusion, **52**, 083001, 2012.
- [5] M. Podesta, et al., Nucl. Fusion, **52**, 033008, 2012.
- [6] S.F. Paul, et al., J. Nucl. Mater. **390-91**, 211-215, 2009.
- [7] R.E. Bell, et al., Rev. Sci. Instrum., **81**, 10D724, 2010.
- [8] B.P. LeBlanc, et al., Rev. Sci. Instrum., **74**, 1659, 2003.
- [9] N.T. Howard, Phys. Plasmas **19**, 056110, 2012.
- [10] W.L. Rowan, et al., Nucl. Fusion **48**, 105005, 2008.
- [11] R. Dux, et al., Nucl. Fusion, **44**, 260-264, 2004.
- [12] R. Dux, et al., Nucl. Fusion, **39**, 1509, 1999.
- [13] R. Dux, et al., Plasma Phys. Control. Fusion, **45**, 1815, 2003.
- [14] C. Giroud, et al., Nucl. Fusion, **313-330**, 2007.
- [15] C. Angioni, et al., Phys. Plasmas, **14**, 055905, 2007.
- [16] M. R. Wade, et al., Phys. Rev. Lett., **84**, 282285, 2000.
- [17] V. A. Soukhanovskii, et al., Plasma Phys. Contr. Fusion **44**, 2339, 2002.
- [18] L. Delgado-Aparicio, et al., Nucl. Fusion, **49**(8):085028, 2009.
- [19] L. Delgado-Aparicio, et al., Nucl. Fusion **51** (8) 083047, 2011.
- [20] D. Clayton, et al., Plasma Phys. Control. Fusion **54**, 105022, 2012.
- [21] S. Kaye, et al., Nucl. Fusion **47**, 499509, 2007.
- [22] S. Kaye, et al., Nucl. Fusion **49** 045010, 2009.
- [23] S. Kaye, et al., Nucl. Fusion **53** 063005, 2013.
- [24] W.A. Houlberg et al., Phys. Plasmas **4** (9), 1997.
- [25] E.A. Belli et al., Plasma Phys. Control. Fusion, **50**, 095010, 2008.
- [26] R. Hulse, Nucl. Technol. Fusion **3** (259), 1983.
- [27] S.P. Hirshmann et al., Nucl. Fusion, **21**, 1079, 1981.
- [28] E.A. Belli et al., Plasma Phys. Control. Fusion, **51**, 075018, 2009.
- [29] E.A. Belli et al., Plasma Phys. Control. Fusion, **54**, 015015, 2012.
- [30] K.L. Wong et al., Phys. Rev. Lett. **59** 2643, 1987.
- [31] K.L. Wong et al. Phys. Fluids B **1** 545, 1989.
- [32] M. Romanelli et al. Plasma Phys. Control. Fusion **40** 1767, 1998.
- [33] J. A. Wesson Nucl. Fusion **37** 577, 1997.
- [34] J.E. Menard, et al. Nucl. Fusion **45** 539, 2005.
- [35] S.P. Gerhardt, et al. Nucl. Fusion **51**, 033004, 2011.
- [36] G. Fussmann, Nucl. Fusion, **26**, 983, 1986.
- [37] K. Wenzel et al., Nucl. Fusion, **30**, 1117, 1990.
- [38] J.M. Canik, et al. Phys. Rev. Lett, **104** (4), 045001, 2010.